Intermediate states of double-beta decay nuclei studied by (n,p) reactions

K. Yako[1], M. Sasano[1], K. Miki[1], M. Dozono[2], K. Hatanaka[3], E. Ihara[2], M. Kato[3], T. Kawabata[4], H. Kuboki[1], Y. Maeda[2], H. Matsubara[3], S. Noji[1], T. Okabe[5], H. Okamura[3], S. Sakaguchi[4], H. Sakai[1], Y. Sasamoto[4], K. Sekiguchi[6], Y. Shimizu[4], K. Suda[3], Y. Tameshige[3], A. Tamii[3] T. Uesaka[4], T. Wakasa[2], and H. Zheng[5]

[1] *Department of Physics, University of Tokyo, Bunkyo, Tokyo 113-0033, Japan*

[2] *Department of Physics, Kyushu University, Higashi, Fukuoka 812-8581, Japan*

[3] *Research Center for Nuclear Physics (RCNP), Osaka University, Ibaraki, Osaka 567-0047, Japan*

[4] *Center for Nuclear Study, University of Tokyo, Bunkyo, Tokyo 113-0033, Japan*

[5] *Institute of Industrial Science (IIS), University of Tokyo, Meguro, 153-8505, Japan*

[6] *The Institute of Physical and Chemical Research (RIKEN), Wako, Saitama 351-0198, Japan*

1 Introduction

The double β decay with two neutrinos in the final state ($2\nu\beta\beta$ decay) is an allowed second-order weak process which has been observed for a number of nuclei. The decay measurements provide the nuclear matrix elements $M^{2\nu}$ which can be compared with the nuclear structure calculations. The understanding of $M^{2\nu}$ is important since it helps one to make reliable predictions of the nuclear matrix elements of neutrino-less double β decay ($0\nu\beta\beta$ decay). If $0\nu\beta\beta$-decay event is observed, it means that the neutrino is a majorana particle whose mass is related to the life time through the nuclear matrix element $M^{0\nu}$.

The double β^- nuclear matrix element of $2\nu\beta\beta$ decay from the initial 0^+ state $|0^{\rm i}_{\rm g.s.}\rangle$ to the final state $|0^{\rm f}_{\rm g.s.}\rangle$ is given by

$$M^{2\nu} = \sum_m \frac{\langle 0^{\rm f}_{\rm g.s.}||O_{\rm GT^-}||1^+_m\rangle\langle 1^+_m||O_{\rm GT^-}||0^{\rm i}_{\rm g.s.}\rangle}{E(1^+_m) - E_0 + 1/2Q_{\beta\beta}}. \quad (1)$$

Here the summation is taken for all 1^+ states in the intermediate nucleus. The Q-value of the $2\nu\beta\beta$ decay is denoted as $Q_{\beta\beta}$, $E(1^+_m) - E_0$ is the energy difference between the m-th intermediate 1^+ state and the initial ground state. The GT operator $O_{\rm GT^-}$ is $\sum_k \sigma_k t^-_k$ taking sum over all the neutrons of the decaying nucleus and it involves spin and isospin transfer ($\Delta S = \Delta T = 1$) without change in angular momentum ($\Delta L = 0$). The deliminator is the product of the Gamow-Teller (GT) matrix element from the mother nucleus to the m-th state in the intermediate nucleus, and that from the m-th state to the ground state of the daughter nucleus. Since the nuclear matrix element depends on details of the wave functions, it is difficult to predict the half lives theoretically so far [1].

Currently two experimental approaches exist aiming at putting constraint on the inputs of the theoretical calculation, such as effective interactions. One is to derive the population of nucleons in the valence orbits which can switch from neutrons to protons by employing stripping or pick-up reactions from mother or daughter nuclei [2]. The other approach is to observe the GT matrix elements in Eq. (1) by means of the charge exchange reactions.

As for ^{48}Ca nucleus, the B(GT) distributions in the low lying states in ^{48}Sc were studied by the high-resolution measurement of ^{48}Ca(^{3}He, t)^{48}Sc reaction at WS course [3] and the ^{48}Ti(d, ^{2}He)^{48}Sc reaction at KVI [4]. A set of similar measurements exist for ^{116}Cd [5, 6]. However, the level density increases with the excitation energy and it is impossible to identify each 1^+ states in the intermediate nuclei. Therefore, we started experimental study of the (p,n) and (n,p) reactions on the double-beta decay nuclei at 300 MeV, from which one can extract the B(GT) distributions in and above the giant resonance regions by multipole decomposition (MD) analysis [7].

In MD analysis, the experimentally obtained angular distributions $\sigma^{\rm exp}(\theta, E_x)$ are fitted using the least-squares method with the linear combination of calculated distributions,

$$\sigma^{\rm calc}(\theta, E_x) = \sum_{\Delta L} a_{\Delta L}\sigma^{\rm calc}_{\Delta L}(\theta, E_x), \quad (2)$$

where the variables $a_{\Delta L}$ are fitting coefficients. The calculated angular distributions for each angular momentum transfer $\sigma^{\rm calc}_{\Delta L}(\theta, E_x)$ are obtained using the distorted wave impulse approximation (DWIA) calculations. It should be noted that at 300 MeV the spin-flip cross sections are large, distortion effects are minimal and therefore the characteristic shapes of the angular distributions for each angular momentum transfer are most distinct. The B(GT) distribution is obtained from $\Delta L = 0$ component of cross section, $\sigma_{\Delta L=0}$, by using the proportionality relation,

$$\sigma_{\Delta L=0}(q,\omega) = \hat{\sigma}_{\rm GT}(q,\omega)B({\rm GT}), \quad (3)$$

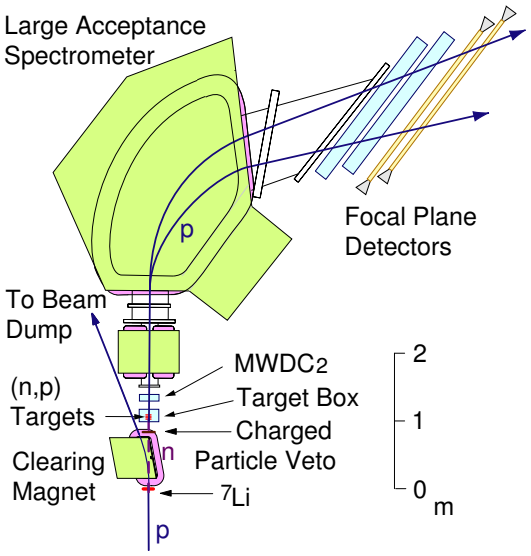

Figure 1: Schematic view of the (n, p) facility.

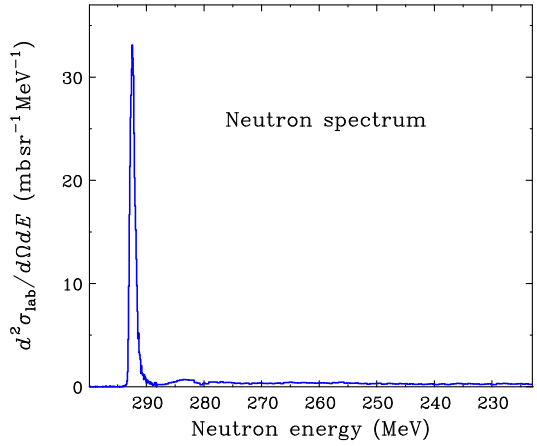

Figure 2: Neutron spectrum produced by the ^{7}Li$(p, n)^7$Be reaction at $\theta = 0°$ and $T_p = 295$ MeV. The peak at 293 MeV is composed of both the ground state and the unresolved first excited state at 0.43 MeV in ^{7}Be.

where $\hat{\sigma}_{GT}$ is the GT unit cross section and $F(q, \omega)$ is the kinematical correction factor which depends on momentum and energy transfers.

Completed the (p, n) measurements on ^{48}Ca and ^{116}Cd [8], we measured the cross section spectra for the ^{48}Ti$(n, p)^{48}$Sc and the ^{116}Sn$(n, p)^{116}$In reactions to study the $B(GT^+)$ distributions up to high excitation energy region of ~ 50 MeV.

2 Experiment at RCNP (n, p) facility

A facility capable of investigating (n, p) reactions at intermediate energies was constructed by utilizing the Large Acceptance Spectrometer (LAS) [9]. The facility allows one to use a relatively thick target in total (~ 0.5 g/cm^2) with a moderate energy resolution of ~ 1 MeV. The effective solid angle and the angular range covered by one spectrometer setting are 11 msr $\pm 2.7°$ and 11 msr, respectively, for an effective target size of $30^{\mathrm{W}} \times 20^{\mathrm{H}}$ mm^2 [10].

The neutron beam is produced from the primary proton beam by a (p, n) reaction. The ejectile neutrons then bombard a secondary target. The recoiled protons due to (n, p) reactions are momentum-analyzed by LAS. A schematic drawing of the facility is shown in Fig. 1.

2.1 Neutron beam

A quasi mono-energetic neutron beam is produced by the ^{7}Li$(p, n)^7$Be(g.s. + 0.43 MeV) reaction, which has a large center-of-mass cross section of 27.0 ± 0.8 mb/sr at 0° over a wide incident energy range of $T_p = 80$–795 MeV [11]. A typical energy spectrum at $T_p = 295$ MeV is shown in Fig. 2. The largest peak in Fig. 2 consists of the ground state and the unresolved 0.43 MeV state in ^{7}Be, which together contribute to the effective neutron beam energy spread of ~ 0.5 MeV.

A proton beam is provided by the high intensity polarized ion source (HIPIS) [12] or NEOMAFIOS ECR ion source [13]. The beam is then accelerated by AVF (Azimuthally Varying Field) and Ring cyclotrons. The beam is transported to the (n, p) facility through the WS course [14].

The primary beam is transported onto the ^{7}Li target and is then bent away by a clearing magnet [15] to the beam dump in the floor 15 m away from the ^{7}Li target. The ^{7}Li target is in the neutron production chamber, which is placed in the pole gap of the clearing magnet. To reduce background events, a charged particle blocker and two collimators are placed inside and outside the vacuum chamber, as shown in Fig. 3. The neutron beam passes through the vacuum window of 10 μm$^{\mathrm{t}}$ aramid and is collimated to $30^{\mathrm{W}} \times 20^{\mathrm{H}}$mm^2 by the outside collimator.

To use the neutron beam efficiently, the distance between the production target and the secondary (n, p) target is designed to be 95 cm, the shortest distance possible. Before entering the (n, p) target box, the neutrons pass through a plastic scintillator with a size of $40^{\mathrm{W}} \times 34^{\mathrm{H}} \times 1^{\mathrm{t}}$ mm^3. Signals from the scintillator are used to veto charged particles coming from the beam line.

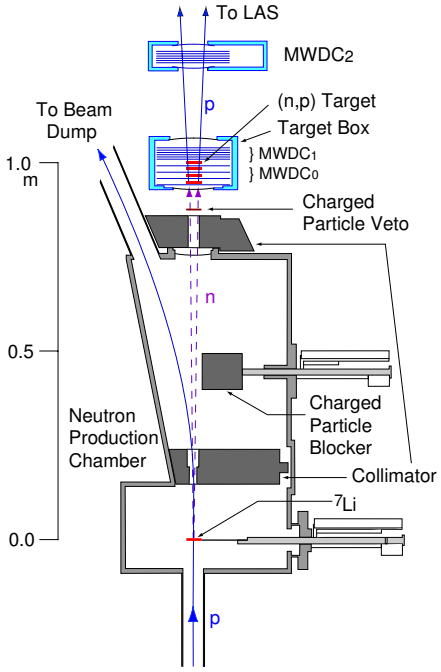

Figure 3: Layout of the neutron production chamber and the MWDCs. The neutron production chamber is located in the pole gap of the clearing magnet.

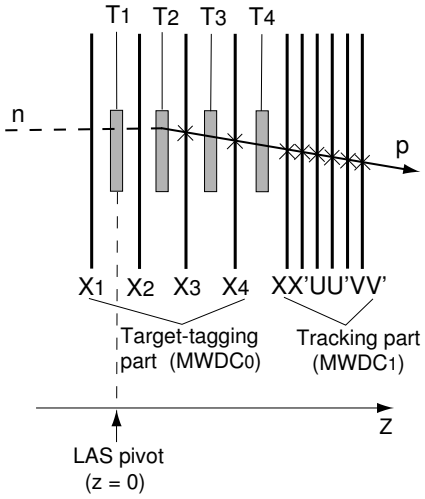

Figure 4: A schematic of the MWDC planes and targets in the target box. An example of an (n,p) event is also shown, where a (n,p) reaction occurs in the second target (T_2) and the outgoing proton hits the MWDC planes downstream.

2.2 (n,p) target system and MWDCs

A segmented (n,p) target is used, which allows for the use of a relatively thick target in total with a moderate energy resolution. Target segments are separated from each other by a plane of multi wire drift chambers ($\mathrm{MWDC_0}$) for identification of the specific target from which a scattered proton is emitted. For tracking purposes, two sets of MWDCs are installed as shown in Fig. 3; $\mathrm{MWDC_1}$ in the target box and $\mathrm{MWDC_2}$ positioned downstream from the target box.

The target system has four target positions separated from one another by the MWDC planes. $T_{1,2,3,4}$, as shown in Fig. 4. The first target, T_1, is positioned on the LAS pivot axis (the designed target position of LAS), while the others are sequentially positioned at intervals of 17 mm. Figure 5 shows the front and the side views of the target box from left to right, respectively. Four vertically oriented target ladders are installed at $T_{1,2,3,4}$ positions. Four targets are mounted on each target ladder and they can be changed individually.

In front of each segment of the target T_i, a $\mathrm{MWDC_0}$ plane X_i is positioned, as shown in Fig. 4. The first wire plane, X_1, positioned just after the entrance window of the target box, may be used to veto charged particles. The other three wire planes, $X_{2,3,4}$, are used to determine the target in which a reaction has occurred.

One advantage of the segmented target system is that events from different targets can be obtained simultaneously. Typically, three targets of interest are positioned in the first three $T_{1,2,3}$ locations, and a polyethylene ($\mathrm{CH_2}$) target is positioned in the most downstream, T_4, position to obtain the $^1\mathrm{H}(n,p)$ data simultaneously. Thus, the measured (n,p) cross sections can be normalized to the well-known $^1\mathrm{H}(n,p)$ cross section [16].

Both $\mathrm{MWDC_1}$ and $\mathrm{MWDC_2}$ consist of 6 wire planes, and each wire plane shares the cathode plane of 6 $\mu\mathrm{m^t}$ carbon-aramid foil. (see Fig. 6). Each wire plane consists of 16 anode wires and 17 field shaping wires alternately stretched out at 2.5-mm intervals. The wires are set vertically for $\mathrm{MWDC_0}$ and for the first two planes of $\mathrm{MWDC_1}$, and thus are sensitive to the horizontal direction (X). The wire positions for the second plane (X') of MWDC1 are shifted by a half cell with respect to the X plane to solve the left-right ambiguities. The wires in the third and fourth planes are inclined by $+45°$ with respect to the vertical axis, and are sensitive to U direction. Similarly, the fifth and sixth planes, inclined by $-45°$, are sensitive to V direction. Therefore the wire configuration of $\mathrm{MWDC_1}$, as a whole, is $XX'UU'VV'$. The wire configuration of $\mathrm{MWDC_2}$, located 25 cm downstream from $\mathrm{MWDC_1}$, is the same as that of $\mathrm{MWDC_1}$, however, it is rotated by 90° around the beam axis; thus, it has a $YY'(-V)(-V)'UU'$ configuration.

The gas in the target chamber is a mixture of Ar (90%) and $\mathrm{CO_2}$ (10%), which is a hydrogen-free, high gain mixture [17]. Chamber gases containing hydrogen are avoided since the $^1\mathrm{H}(n,p)$ reaction would give rise to a large background. Anode signals are preamplified by REPIC RPV-041, and then amplified and discriminated by LeCroy 2735DC. The time information is digitized by LeCroy 3377 TDCs.

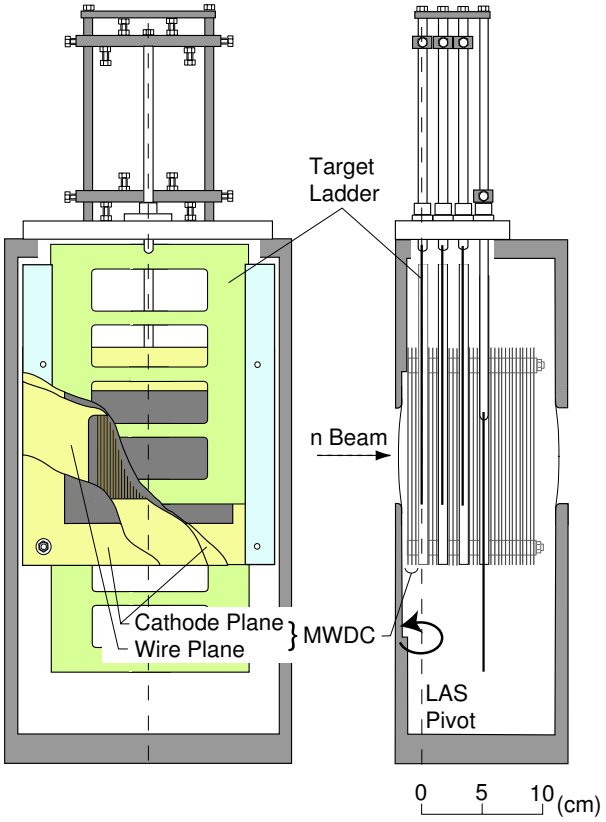

Figure 5: Front and side views of the (n, p) target box.

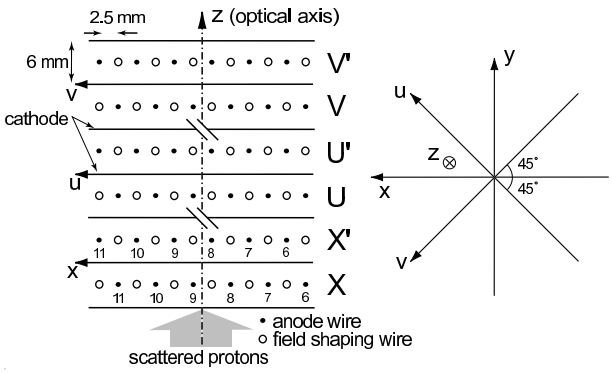

Figure 6: Wire configuration of MWDC_1.

The hit-rate of each plane was typically 500 kHz, mainly due to the protons from the ^{7}Li target. An efficiency of $> 97\%$ and a position resolution of 0.4 mm per plane were maintained throughout the measurements.

2.3 Targets

The typical beam intensity was 300 nA and the thickness of the ^{7}Li target was 320 mg/cm^2, which produced 2×10^6 neutrons/s on the effective target region. Three ^{116}Sn targets with thicknesses of 406, 338, and 419 mg/cm^2 and a polyethylene (CH_2) target with a thickness of 46 mg/cm^2 were mounted in the (n, p) target box. The number of $^1\mathrm{H}(n, p)$ events from the CH_2 target was used for normalization of the neutron flux. In the measurements of $^{48}\mathrm{Ti}(n, p)$ reaction, three ^{48}Ti targets of ~ 300 mg/cm^2 and a ^{7}Li target of 210 mg/cm^2 were used. Blank target data were also taken for background subtraction.

3 Result – current status and perspective

We have obtained the double differential cross sections up to 40 MeV excitation energy over an angular range of 0°–12° in the laboratory frame. Figures 7 and 8 show some of the obtained spectra for the $^{48}\mathrm{Ti}(n, p)$ and $^{116}\mathrm{Sn}(n, p)$ reaction, respectively. The overall energy resolutions estimated from the target thicknesses are 1.2 MeV for the $^{48}\mathrm{Ti}(n, p)$ spectra and 1.4 MeV for the $^{116}\mathrm{Sn}(n, p)$ spectra. The upper panels show the spectra at 0°, where the $\Delta L = 0$ component of the cross section is at maximum while the lower panels show those at angles where the $\Delta L = 1$ component take the maximum cross section. There are two peaks in Fig. 7 at 3 MeV and 6 MeV. The amplitude of the 3-MeV peak decreases with angle and this peak can be attributed to GT 1^+ states observed also in the previous (n, p) and $(d, ^2\mathrm{He})$ measurements [18, 4]. The cross section of 6-MeV peak does not change much with angle, but might contain some $\Delta L = 0$ component although Ref. [18] attributes it mainly to the $\Delta L = 1$ transition. The $^{116}\mathrm{Sn}(n, p)$ spectra have no clear indication of forward-peaking GT contribution except the ground state for which the $B(\mathrm{GT})$ is known to be 0.256 ± 0.001 [19]. The multipole decomposition analysis will be performed to identify the GT component of the cross in the continuum.

GT excitations in (n, p)-type reactions on $N > Z$ nuclei are blocked due to the Pauli-blocking of states which are occupied in neutron-rich nuclei. Therefore the $B(\mathrm{GT}^+)$ distributions studied in this work are more sensitive to the ground state correlations than the $B(\mathrm{GT}^-)$ distributions. It will be interesting to compare the whole

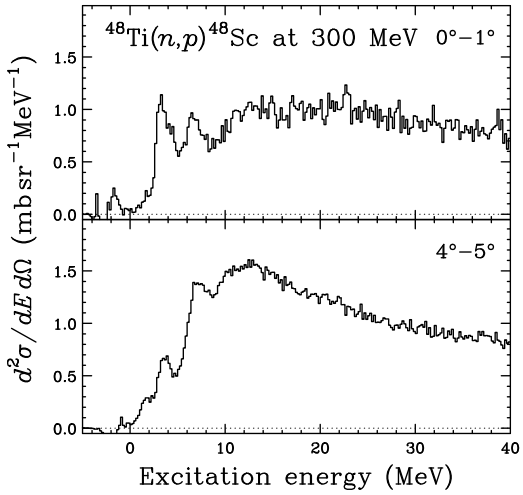

Figure 7: Double differential cross sections for the ^{48}Ti(n,p) reaction at 300 MeV as a function of the excitation energy in ^{48}Sc and the reaction angle.

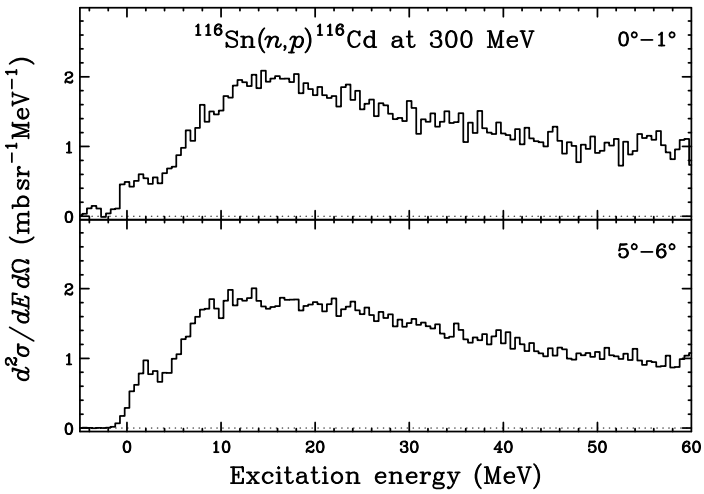

Figure 8: Double differential cross sections for the ^{116}Sn(n,p) reaction at 300 MeV as a function of the excitation energy in ^{116}In and the reaction angle.

$B(\mathrm{GT}^+)$ distributions with theoretical predictions since the data will constrain the inputs of the calculations more stringently.

4 Summary

We performed the measurements of the ^{48}Ti(n,p) and ^{116}Sn(n,p) reaction to study the distributions of β^+ GT strength which contribute to the decay process of ^{48}Ca and ^{116}Cd, respectively. The (n,p) facility is described. It produces 2×10^6 neutrons/s on an effective target region of $30^{\mathrm{W}}\times20^{\mathrm{H}}\mathrm{mm}^2$ in a typical run condition. The angular range and the solid angle covered by one spectrometer setting are $\pm2.7^\circ$ and 11 msr, respectively.

References

[1] For example, J. Suhonen and O. Civitarese, Phys. Rep. **300**, 123 (1998).
[2] J.P Schiffer et al., Phys. Rev. Lett. **100**, 112501 (2008).
[3] E.-W. Grewe et al., Phys. Rev. C **77**, 064303 (2008).
[4] S. Rakers et al., Phys. Rev. C **70**, 054302 (2004).
[5] H. Akimune et al., Phys. Lett. B, in press, doi:10.1016/j.physletb.2008.02.046; H. Akimune et al., Phys. Lett. B **394**, 23 (1997).
[6] S. Rakers et al., Phys. Rev. C **52**, 604 (2005).
[7] M. Ichimura, H. Sakai, and T. Wakasa, Prog. in Part. and Nucl. Phys. **56**, 446 (2006). N. Matsuoka et al., RCNP Annual Report 1990, pp. 235.
[8] M. Sasano et al., Nucl. Phys. A, **788**, 76c (2007).
[9] N. Matsuoka, T. Noro, RCNP Annual Report 1987, pp. 176; N. Matsuoka et al., RCNP Annual Report 1990, pp. 235.
[10] K. Yako et al., Nucl. Instr. and Meth. A, **592**, 88 (2008).
[11] T.N. Taddeucci et al., Phys. Rev. C 41 (1990) 2548.
[12] K. Hatanaka et al., Nucl. Instrum. Meth. A 384 (1997) 1575.
[13] K. Takahisa et al., RCNP Annual Report 1996, pp. 170.
[14] T. Wakasa et al., Nucl. Instrum. Meth. A, 482 (2002) 79.
[15] J. Kamiya et al., RCNP Annual Report 1998, pp. 113.
[16] R.A. Arndt et al., Phys. Rev. D 28 (1983) 97; R.A. Arndt et al., Scattering Analysis Interactive Dial-in program (SAID), http://gwdac.phys.gwu.edu.
[17] For example, F. Sauli, "Principles of Operation of Multiwire Proportional and Drift Chambers", CERN Report (1977) 77-09.
[18] W.P. Alford et al., Nucl. Phys. A **514**, 49 (1990).
[19] M. Bhattacharya, et al., Phys. Rev. C **58**, 1247 (1998).